

Crystallinity and composition engineering of organic crystal derived 1D carbons for advanced Li-metal based batteries

Minsu Park ^a, Kwonyun Lee ^b, Min Sung Kang ^c, Sujeong Woo ^a, Wootaek Choi ^a, Hyein Kim ^b, Woong Kwon ^b, Junghyun Choi ^d, Sung Beom Cho ^{c,***}, Euigyung Jeong ^{b,**}, Patrick Joohyun Kim ^{a,*}

^a Department of Applied Chemistry, Kyungpook National University, Daegu, 41566, Republic of Korea

^b Department of Textile System Engineering, Kyungpook National University, Daegu, 41566, Republic of Korea

^c Department of Materials Science and Engineering and Department of Energy Systems Research, Ajou University, Suwon-si, 16499, Republic of Korea

^d School of Chemical, Biological and Battery Engineering, Gachon University, Seongnam-si, Gyeonggi-do, 13120, Republic of Korea

ARTICLE INFO

Keywords:

Organic pigment
Carbonization
N-rich carbon
Lithiophilicity
Li metal

ABSTRACT

Lithium (Li) has garnered considerable interest in the battery industry owing to its outstanding theoretical capacity (3860 mAh g^{-1}) and low redox potential (-3.04 V vs. standard hydrogen electrode). Unfortunately, the practical applications of Li-metal batteries (LMBs) are impeded by low coulombic efficiency and dendritic Li formation during the charging/discharging process. One of viable strategies for overcoming these challenges involves the use of N-rich carbons in designing functional separators and current collectors. In this study, the potential of organic crystal material (Pigment Red 122; PR122) as a carbonizable nitrogen-rich material was investigated to assess its impacts on the electrochemical performance of Li-ion batteries (LIBs) and LMBs. The carbonization temperature of PR122 was precisely controlled to alter the overall content of nitrogen element in the carbon backbone. Each prepared N-rich carbon was applied to modify the surface of each separator and current collector. The PR122-derived carbon pyrolyzed at a high temperature of $1500 \text{ }^\circ\text{C}$ (PR|C1500) demonstrated lower discharge capacity. However, it exhibited better electrochemical kinetics than the PR122-derived carbon pyrolyzed at a lower temperature of $600 \text{ }^\circ\text{C}$ (PR|C600) in LIBs. In the case of LMBs, the Li/Cu cell with a PR|C600 coated separator delivered better cycle stability than the Li/Cu cell with a PR|C1500 coated separator. These results suggest that both the nitrogen content (specifically pyridinic-N and pyrrolic-N) and degree of crystallinity in the carbon platform significantly affect the electrochemical stability and kinetics of LIBs and LMBs. The foregoing is further verified by analysis using the density functional theory-based finite element method.

1. Introduction

In recent years, the growing concerns worldwide have led to increased attention on reducing CO_2 emissions, which are the primary cause of global warming. For this reason, electric vehicles (EVs) have been receiving steady attention as an alternative to fossil fuel-based

vehicles for reducing CO_2 emissions [1–3]. Li-ion batteries (LIBs), currently the most commercially available EV batteries, have the advantages of long cycle life, low self-discharge rate, and reliability [4–6]. However, there is a growing interest in high-capacity, rechargeable batteries due to the increase in demand for long-range EVs [7,8]. Despite the well-established use of graphite with a capacity of 372 mAh g^{-1} as

Abbreviations: LIBs, Li-ion batteries; LMBs, Li-metal batteries; PR122, Pigment red 122; PVDF, Polyvinylidene fluoride; NMP, 1-methyl-2-pyrrolidone; EC, Ethylene carbonate; DEC, Diethyl carbonate; SEM, Scanning electron microscopy; EDS, Energy dispersive spectroscopy; EA, Elemental analysis; XPS, X-ray photoelectron spectroscopy; XRD, X-ray diffraction; BET, Brunauer emmett teller; EIS, Electrochemical impedance spectroscopy; GITT, Galvanostatic intermittent titration technique; CV, Cyclic voltammetry.

* Corresponding author.

** Corresponding author.

*** Corresponding author.

E-mail addresses: csb@ajou.ac.kr (S.B. Cho), wolfpack@knu.ac.kr (E. Jeong), pjkim@knu.ac.kr (P.J. Kim).

<https://doi.org/10.1016/j.carbon.2024.119870>

Received 11 September 2024; Received in revised form 16 November 2024; Accepted 26 November 2024

Available online 28 November 2024

0008-6223/© 2024 Elsevier Ltd. All rights are reserved, including those for text and data mining, AI training, and similar technologies.

the anode material in LIBs, the necessity for research on batteries with higher capacities is growing due to the increasing demand for such batteries.

Metallic Li is considered as a promising anode material due to their high capacity (3860 mAh g⁻¹) and low redox potential (-3.04 V vs. standard hydrogen electrode) [9–11]. However, uneven distribution of Li-ion flux and uncontrollable growth of Li dendrites stem from the host-less feature of Li metal anode [12,13]. The Li dendrites promote the formation of a disrupted solid electrolyte interphase (SEI) layer, accelerating the consumption of active Li [14–16]. This reduces the electrochemical reversibility, consequently decreasing the cycle life of the battery [17,18]. Furthermore, Li dendrites penetrate the separator, leading to battery short-circuits and thermal runaway [19,20].

Numerous studies have been explored to address these issues such as passivating the surface of Li-metal anodes [21–23], adopting the system of solid-state electrolytes [24–26], stabilizing the surface stability through forming artificial SEI layers [27–29], modifying the surface of separators and current collectors using carbon materials. Carbon materials such as carbon paper [30–32], carbon nanotubes [33–35], graphite/graphitized carbon [36,37], and graphene [38,39] are notable for enhancing the electrochemical reversibility within batteries. However, intrinsic carbons with very few defects exhibit Li-phobic characteristics, which can contribute to uneven Li deposition and the growth of Li dendrites [40,41]. The introduction of additional Li-affinitive modification such as nitrogen doping to carbon material surfaces is one strategy to promote uniform Li-deposition [42–44]. Nitrogen within the carbon structure facilitates the uniform distribution of Li nuclei through its unshared electron pairs [45,46]. Furthermore, the pyridinic and pyrrolic nitrogen within N-rich carbon structures exhibit strong interactions with Li atoms [47–49]. This facilitates the adsorption of Li ions into the carbon structure, controlling the Li-ion flux and resulting in uniform Li deposition.

In this study, we explored the organic crystal material (C.I. Pigment Red 122 (PR122)) as a carbonizable precursor for nitrogen (N)-rich carbon to investigate how the structure of carbonized PR122 affects the electrochemical kinetics and stability of LIBs and LMBs. The introduction of PR122 as a precursor for N-rich carbons has several advantages. First, PR122 naturally contains heteroatoms such as nitrogen, eliminating the need for additional post-treatment to introduce heteroatoms into the carbon structure [50,51]. Second, PR122 enables convenient modulation of heteroatom content, such as nitrogen and oxygen, by controlling the carbonization temperature [52,53]. Lastly, by leveraging its ability to modify heteroatom content and crystallinity through changes in the carbonization protocol, PR122 can be effectively integrated into various Li-metal-based battery systems [53,54]. PR122-derived carbon pyrolyzed at 600 °C (PR|C600) has the highest heteroatom content among carbon materials processed under different temperature conditions, with nitrogen and oxygen contents of 8 % and 4 %, respectively. In contrast, PR122 pyrolyzed at 1500 °C (PR|C1500) contains relatively few heteroatoms, with nitrogen accounting for only 1.28 %. Instead, the carbon structure rearranges, leading to increased crystallinity as the functional groups are removed [55,56]. In the LIB system, PR|C1500 showed the highest electrical and ionic conductivity compared with other samples; this is attributed to its high crystallinity. However, due to the absence of heteroatoms to interact with Li ions, it exhibits low specific capacity values. Each PR122 derived 1D carbon with different nitrogen content was coated on polypropylene (PP) separators to evaluate electrochemical properties in LMBs. The Li/Cu cell with PR|C600-coated separator exhibited the best cycle performance among the cells, due to the uniform Li deposition enabled by the high nitrogen content of PR|C600. The results were meticulously confirmed by observing the morphology of surface-deposited Li via scanning electron microscopy (SEM) and further supported by density functional theory (DFT) calculations and finite element method (FEM) analysis.

2. Experimental section

2.1. Material preparation and characterization

C.I. PR122 (Cinquasia® Magenta D 4550 J, BASF) was used as 2,9-dimethyl quinacridone. It was carbonized at 600, 1050, and 1500 °C for 1 h under N₂ atmosphere. The morphologies of the carbonized PR122 samples and Li-plated carbonized PR122 separators were examined using field-emission SEM (Hitachi, SU8220) and energy-dispersive X-ray spectroscopy (EDS, Ultim Max100, OXFORD). Elemental analysis was conducted using an elemental analyzer (ThermoFisher, FlashSMART) to determine the elemental ratios of C, N, O, and H in the PR122 samples as a function of carbonization temperature. To identify the nitrogen and oxygen functional groups on the surface of the carbonized PR122 samples, X-ray photoelectron spectroscopy (XPS, ThermoFisher, NEXSA) was conducted. Raman spectra measurement was conducted by raman spectrometer (Renishaw, inVia reflex) to determine the crystallinity of the carbonized PR122 samples. The X-ray diffraction (XRD, Panalytical, EMPYREAN) was performed to analyze the crystallographic structures of the carbonized PR122 samples. N₂ adsorption and desorption and pore distribution measurements of the carbonized PR122 samples were carried out using Brunauer–Emmett–Teller (BET, Quadasor evo, Quantachrome) analyzer.

2.2. Evaluation in the LIB system

2.2.1. Preparation of LIB electrodes using PR|C600, PR|C1050, and PR|C1500

To prepare the slurries for each electrode, 80 wt % each carbonized PR122, 10 wt % Super P, 10 wt % binder (polyvinylidene fluoride, PVDF) was homogenized with 1-methyl-2-pyrrolidone (NMP, 99.5 %, SAMCHUN) by the planetary mixer (AR-100, THINKY). The prepared slurries were laminated on the copper foil via tape casting, followed by overnight drying in a convection oven at 50 °C. Thereafter, the fully dried laminated copper foils were cut into circular disks each with diameters of 12 mm for coin-cell assembly. The actual active masses of PR|C600, PR|C1050, and PR|C1500 are 0.86 mg cm⁻², 0.87 mg cm⁻², 0.88 mg cm⁻², respectively.

2.2.2. Electrochemical measurements

Standard 2032R-type coin cells were fabricated in a glove box filled with Ar gas to evaluate the electrochemical performance using 1.0 T Li foil as the counter electrode. In addition, 1.0 M LiPF₆ in ethylene carbonate (EC) and diethyl carbonate (DEC) with a volume ratio of 1:1 was used as an electrolyte. The cycle performance, voltage profiles, and rate capabilities of each cell were assessed within the voltage window from 0.001 V to 2 V. The Li-ion diffusion coefficient was calculated via galvanostatic intermittent titration technique (GITT) by applying a pulse current (0.2 A g⁻¹) for 10 min, followed by open-circuit mode for 10 min within a potential window of 0.001–2V vs. Li/Li⁺. Electrochemical impedance spectroscopy (EIS, Biologic, SP-150e) was conducted with an amplitude of 10 mV at a frequency range of 200 kHz–10 mHz. Cyclic voltammetry (CV) measurements were recorded between 0.001 and 2 V (vs. Li/Li⁺).

2.3. Evaluation in the Li-metal battery system

2.3.1. Preparation of modified separators

90 wt % each carbonized PR122 and 10 wt % PVDF binder were mixed with NMP by the planetary mixer. The prepared slurries were laminated on the PP separator (2400, Celgard) via tape casting and dried in a convection oven at 50 °C, overnight. For the coin-cell assembly, the carbonized PR-coated separators were cut into circular disks each with a diameter of 18 mm.

2.3.2. Electrochemical measurements

The electrochemical performance of LMB systems was also evaluated using standard 2032R-type coin cells fabricated in a glove box filled with Ar gas. An electrolyte containing 1 M LiPF₆ in EC:DEC at a 1:1 vol. was used, and 1.0 T Li foil was employed as the counter electrode for coin cell assembly. The Li deposition process was carried out at an areal capacity of 1.0 mAh cm⁻² with the cut-off voltage for the Li dissolution process set at 1.0 V. The Li/Cu cells with modified separators were evaluated at constant current densities of 1.0 mA cm⁻².

2.4. DFT calculations

The DFT was performed with the Vienna ab-initio simulation package (VASP) [57], utilizing the projector augmented wave (PAW) method [58]. The Perdew-Burke-Ernzehof (PBE) exchange–correlation functional within the framework of the generalized gradient approximation (GGA) was employed in the DFT calculations [59]. The cut-off energy for plane wave expansion was set to be 520 eV. The Brillouin zone was sampled by employing 2 × 2 × 1 k-point grids in the reciprocal space for the geometry optimizations. The adsorption energy (E_{ads}) of Li on surfaces was defined as:

$$E_{ads} = E_{System} - (E_{Surface} + E_{Li}) \quad (1)$$

where, E_{Surface} was the total energy of surfaces, E_{Li} was the total energy of the isolated Li atom, and E_{System} was the total energy of a system consisted of Li atom adsorbed on surfaces. A negative E_{ads} value indicates a favorable adsorption.

2.5. FEM simulation

The finite element method (FEM) simulations were performed using COMSOL Multiphysics 6.2 software to study the Li-deposition behavior in the Li/Cu asymmetric cell. To simulate the Li-flux variations inside the cell during the charging process and the morphology of Li-deposition on the electrode, we incorporated various physical models such as electrochemistry and species transport. The specific parameters used in the modeling are summarized in Table S1.

2.5.1. Electrochemistry

Electrochemistry was determined using the secondary current distribution method, which account for concentration gradients and electrode kinetics. In the model, the charge transport in an electrolyte was assumed to follow Ohm's law:

$$\mathbf{i}_l = -\sigma_l \nabla \phi_l \quad (2)$$

$$\nabla \cdot \mathbf{i}_l = 0 \quad (3)$$

Where \mathbf{i}_l is the current density vector, σ_l is the electrical conductivity, and ϕ_l is the electrolyte potential. Moreover, the lateral boundaries of geometry were set to null electric flux to ensure periodicity:

$$-\mathbf{n} \cdot \mathbf{i}_l = 0 \quad (4)$$

Where \mathbf{n} is the normal vector.

In particular, to describe the current density on the surface and the overpotential, the electrodes were defined with concentration-dependent kinetics, which can be expressed by Butler-Volmer equation:

$$i_{loc} = i_o \left[c_R \exp\left(\frac{\alpha_a F \eta}{RT}\right) - c_O \exp\left(\frac{\alpha_c F \eta}{RT}\right) \right] \quad (5)$$

where i_{loc} is the local charge transfer current density, i_o is the exchange current density, c_R and c_O are the concentration of reduced and oxidized species, respectively, F is the Faraday's constant, η is the overpotential, R is the gas constant, α_a and α_c are the charge transfer coefficients of the anodic and cathodic, respectively.

2.5.2. Transportation of species

The mass transfer equation accounting for transport of diluted species in an electrolyte is described by the Nernst-Planck equation:

$$\frac{\partial c_i}{\partial t} + \nabla \cdot \mathbf{J}_i = 0 \quad (6)$$

where c_i is the concentration of an ionic species i , and \mathbf{J}_i is the flux of species i . In this model, we considered that the charged chemical ions are transported by diffusion and migration. Thus, the ionic flux can be expressed as:

$$\mathbf{J}_i = -D_i \nabla c_i - \frac{D_i z_i F}{k_B T} c_i \nabla \phi_i \quad (7)$$

where D_i is the diffusion coefficient of diluted species i , z_i is the valence charge, and k_B is the Boltzmann constant. The first term on the right side of Eq. (7) represents the diffusive flux driven by concentration gradient, and the second term indicates the electromigration influenced by the electric field.

3. Results and discussion

As shown in Fig. 1, PR122 was carbonized in N₂ atmosphere at temperatures of 600, 1050, and 1500 °C. The PR122 has the structure of 2,9-dimethylquinacridone (DMQA), which is an aromatic compound consisting of pentacene with methyl groups bonded to corner benzene rings. The N–H and C=O groups in the aromatic compound consisting of five linear benzene rings are located at various positions, promoting intermolecular hydrogen bonding. In addition, the carbon backbone of 2,9-DMQA facilitates π-π stacking interactions, resulting in high crystallinity, like organic crystals [52,60,61]. The methyl functional group is separated at pyrolysis temperatures above 450 °C, which forms polycyclic aromatic hydrocarbons with parallel-aligned longitudinal microstructures that contribute to the formation of the fiber-like structure. The oxygen in the DMQA is decomposed at pyrolysis temperatures approximately 600 °C, releasing impurities such as H₂O, CO, O₂, and CO₂ [62]. The nitrogen in the DMQA is decomposed to produce NH₃ as a byproduct in which pyrolysis occurs at temperatures exceeding 800 °C. The structure is rearranged, resulting from the decomposition of the methyl, carbonyl, and amine functional groups present on the 2,9-DMQA backbone. The obtained fiber structure consists of disordered carbon, and the presence of heteroatoms varies depending on the pyrolysis temperature. These carbonized materials are referred to as PR|C600, PR|C1050, and PR|C1500, respectively.

The surface morphology of PR122 carbonized under a series of conditions are shown in Fig. 2. The digital image of PR122 before and after carbonization are depicted in Fig. 2a. PR122, a pigment used to represent colors in the magenta family, transforms into a gray color upon carbonization. The SEM images of PR122 are provided in Fig. 2b and c. PR122 exhibits an agglomerated morphology with spherical particles ranging in size from 2 to 5 μm. The low-magnification SEM images of PR|C600, PR|C1050, and PR|C1500 are shown in Fig. 2d–f. The carbonized PR122 consists of one-dimensional carbon network. The transformation of PR122 into different forms after carbonization is due to the continuous succession of cyclic aromatic structures into a fiber morphology. The two methyl functional groups present in PR122 decompose thermally, linking the aromatic backbones of each PR122 monomer. In addition, the thermal decomposition of carbonyl and amine groups contributes to the rearrangement of the structure at higher carbonization temperatures, resulting in various morphologies. High-magnification SEM images reveal that the structure is predominantly composed of fiber-like formations (Fig. 2g–i). The nitrogen distribution in PR|C600, PR|C1050, and PR|C1500, examined through EDS mapping, are presented in Fig. 2j–l. However, PR|C1500 exhibits the lowest nitrogen content across the entire surface area, due to the release of nitrogen at 800 °C and its subsequent decomposition at the pyrolysis

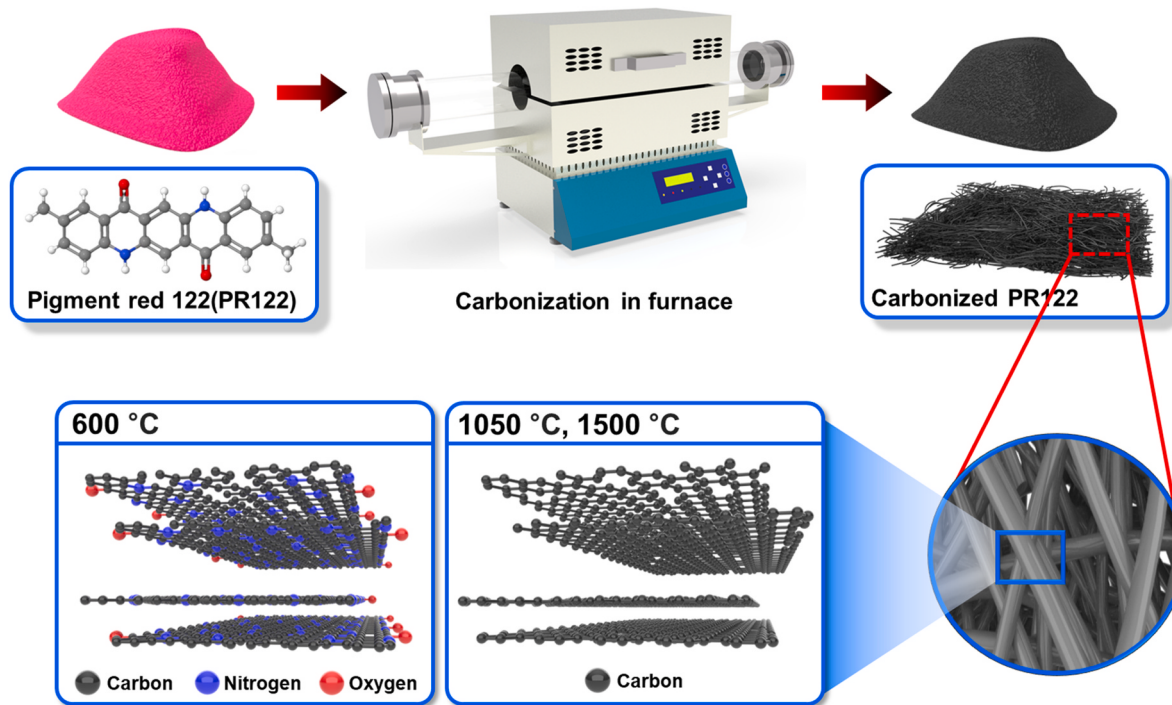


Fig. 1. Concept. Schematic illustration to depict the process for preparation of PR122-derived 1D carbons.

temperature of 1500 °C [63–65].

The nitrogen contents in PR|C600, PR|C1050, and PR|C1500, as determined by elemental analysis, are summarized in Fig. 3a and Table S2. The nitrogen percentages in the PR|C600, PR|C1050, and PR|C1500 samples are 8.64 wt %, 3.12 wt %, and 1.28 wt %, respectively. The XPS survey spectra are presented in Fig. 3b and c. The peak at ~286 eV corresponds to the binding energy of C 1s. The peak at ~530 eV representing the O 1s region and the peak at ~400 eV corresponding to the N 1s gradually disappear as the pyrolysis temperature increases. To gain insights into their nitrogen bonds, the N 1s spectra of each PR|C600, PR|C1050, and PR|C1500 are deconvoluted; these are presented in Fig. 3d–f, respectively. The spectra of the three samples exhibit peaks at ~398, ~400, and ~402 eV, corresponding to pyridinic N, pyrrolic N, and graphitic N, respectively [66,67]. As the carbonization temperature increases, the peak intensities corresponding to pyrrolic N and pyridinic N become significantly lower compared to graphitic N [52,53]. This indicates that graphitic N has a lower formation energy compared with other nitrogen forms, making it relatively more stable and less prone to thermal decomposition [68]. The structural changes of PR122 with varying carbonization temperatures were analyzed via Raman spectroscopy, as shown in Fig. 3g. The I_D/I_G ratios of carbonized PR122 are 0.88, 0.87, and 0.85 for PR|C600, PR|C1050, and PR|C1500, respectively. The relative intensity of the D peak, corresponding to the disorder band, gradually decreases. This indicates that the carbon structure becomes more ordered with increasing carbonization temperature. The XRD pattern of each sample is displayed in Fig. 3h. The carbonized PR122 exhibits two broad peaks at approximately 25° and 43°, corresponding to the (002) and (100) crystallographic planes, respectively, indicative of a soft carbon structure [69]. The fullwidth at half the maximum (FWHM) values for PR|C600, PR|C1050, and PR|C1500 are 0.108, 0.099, and 0.062, respectively. According to Scherrer's equation, crystal size is inversely proportional to the FWHM value of the peak, indicating that PR|C1500 has the highest crystallinity with fewer defects associated with the presence of heteroatoms [70]. The variation in functional groups according to the degree of carbonization of PR122, as determined by Fourier transform infrared (FT-IR) analysis, is illustrated in Fig. 3i. The peaks at ~1340 cm⁻¹, ~1650 cm⁻¹, and ~3400 cm⁻¹

represent C–N in aromatic amine, C=O, and N–H in secondary amine, respectively. The N–H functional group disappears at 600 °C, and the carbonyl group and C–N bond disappear over 1050 °C. The infrared curve for PR|C1050 flattens, indicating that most of the heteroatoms have disappeared as the carbonization temperature exceeds 1050 °C. The N_2 adsorption/desorption and pore size distributions of PR|C600, PR|C1050, and PR|C1500 are shown in Figs. S1a and S1b. The isotherm curves exhibit type-IV characteristics, indicating that the carbonized PR122 possesses both meso- and macroporous structures. The pore size distribution for all three carbonized PR samples ranges from 25 to 150 nm, with macropores predominantly comprising the distribution. The specific surface areas of PR|C600, PR|C1050 and PR|C1500 are 65.26 m² g⁻¹, 61.74 m² g⁻¹ and 51.02 m² g⁻¹, respectively.

The electrochemical properties of PR|C600, PR|C1050, and PR|C1500 in the LIB system are presented in Fig. 4. As shown in Fig. 4a, the cycling behaviors of each electrode were assessed over 100 cycles at a current density of 0.2 A g⁻¹. The reversible discharge capacities of PR|C600, PR|C1050, and PR|C1500 are 440.2, 316.0, and 247.2 mAh g⁻¹, respectively. This result suggests that nitrogen atoms in the carbon structure interact with Li ions due to higher electronegativity compared to carbon, facilitating efficient Li-ion storage [67,71]. Table S3 compares the specific capacities of various carbon anode materials reported in other works. The voltage profiles of the 1st, 10th, 50th, and 100th cycle for each electrode at 0.2 A g⁻¹ are depicted in Fig. 4b–d. The discharge capacity of the three anodes in the first cycle exhibits much higher values than in the subsequent cycles due to the formation of the SEI layer and Li insertion into the carbon backbone [67]. For this reason, the voltage plateaus for PR|C600, PR|C1050, and PR|C1500 appear at 1.0 V, 0.7 V, and 0.6 V, respectively. The three cells stabilize after 10 cycles with slight decrease in discharge capacity. The rate retention of each electrode at different current densities ranging from 0.1 to 10 A g⁻¹ for four repeated cycles is shown in Fig. 4e. At the current density of 0.1 A g⁻¹, the PR|C600 shows the highest discharge capacity of 615.9 mAh g⁻¹. However, it exhibits the lowest rate retention characteristics and shows the lowest capacity at the current density of 10 A g⁻¹ (54.7 mAh g⁻¹). The PR|C1500 exhibits a lower discharge capacity value of 295.3 mAh g⁻¹ at 0.1 A g⁻¹ compared with the other electrodes. Interestingly,

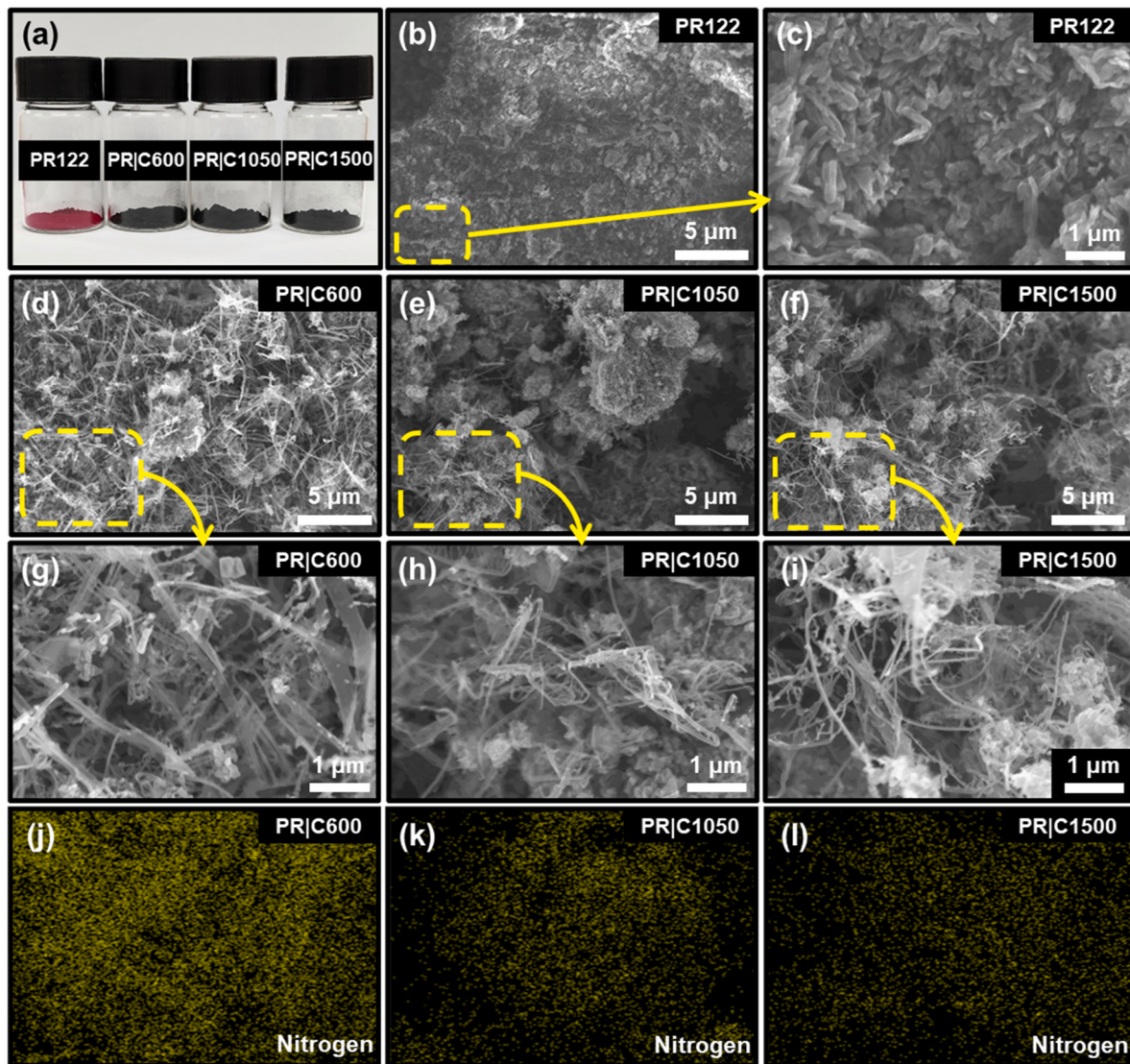


Fig. 2. Morphology. (a) Digital image of PR122, PR|C600, PR|C1050, PR|C1500 powders. Top-view SEM images of PR122 at (b) low and (c) high magnification. Top-view SEM images of PR|C600, PR|C1050, and PR|C1500 at (d–f) low and (g–i) high magnification. (j–l) Nitrogen EDS mapping of PR|C600, PR|C1050, and PR|C1500.

PR|C1500 shows the highest discharge capacity (126.5 mAh g^{-1}) at the current density of 10 A g^{-1} compared with the other electrodes and demonstrates the best rate retention characteristics. Extrapolating from the above results, it can be inferred that PR|C1500 has the fewest nitrogen-associated defects due to its high carbonization temperature, resulting in a relatively stable electrochemical kinetics and improved Li-ion diffusion. In contrast, while the nitrogen in PR|C600 provides large adsorption sites for Li ions, the heteroatoms act as defects in the crystal structure, leading to poor Li-ion diffusion. The voltage profiles representing the rate retention of each electrode are shown in Fig. 4f–h. The PR|C600 exhibits a rapid decrease in discharge capacity as the current density increases. The PR|C1050 cell shows a rapid decrease in discharge capacity at 2 A g^{-1} , whereas the PR|C1500 shows a smaller decrease in discharge capacity than the other two electrodes. These results demonstrate that the high nitrogen content in the carbon structure of PR122 provides a number of sites for Li storage. However, when the nitrogen content is excessive, it can act as a defect within the carbon structure, thereby reducing the electrochemical kinetics.

The impact of the carbonization temperature of PR122 on Li-ion diffusivity, ionic conductivity, and interfacial impedance is meticulously evaluated. The GITT curves for PR|C600, PR|C1050, and PR|

C1500 are presented in Fig. 5a and b. The IR drops of each PR|C600, PR|C1050, and PR|C1500 are 0.032 V , 0.030 V , and 0.024 V , respectively. The PR|C1500 exhibits the smallest IR drop among the cells, indicating the lowest internal resistance of the electrodes. The Li-ion diffusion coefficient (D_{Li}) for each cell can be calculated using Fick's second law according to the following equation:

$$D_{Li} = \frac{4}{\pi \tau} \left(\frac{m_b}{\rho S} \right)^2 \left(\frac{\Delta E_s}{\Delta E_r} \right)^2, \quad (8)$$

where τ is the time of the current pulse; m_b is the molar mass; ρS is the density of the host material; ΔE_s is the steady-state voltage variation; and ΔE_r represents the total voltage variation during a single galvanostatic titration step. The average diffusion coefficients for PR|C600, PR|C1050, and PR|C1500 were determined to be $8.34 \times 10^{-10} \text{ cm}^2 \text{ S}^{-1}$, $6.45 \times 10^{-9} \text{ cm}^2 \text{ S}^{-1}$, and $5.84 \times 10^{-8} \text{ cm}^2 \text{ S}^{-1}$, respectively, note that PR|C1500 exhibits the highest value. These results suggest that the stiffening of the crystal structure, induced by high carbonization temperatures, significantly enhances ionic conductivity. As the carbonization temperature increases, the carbon structure becomes more rigid and orderly, reducing the number of defects and facilitating smoother

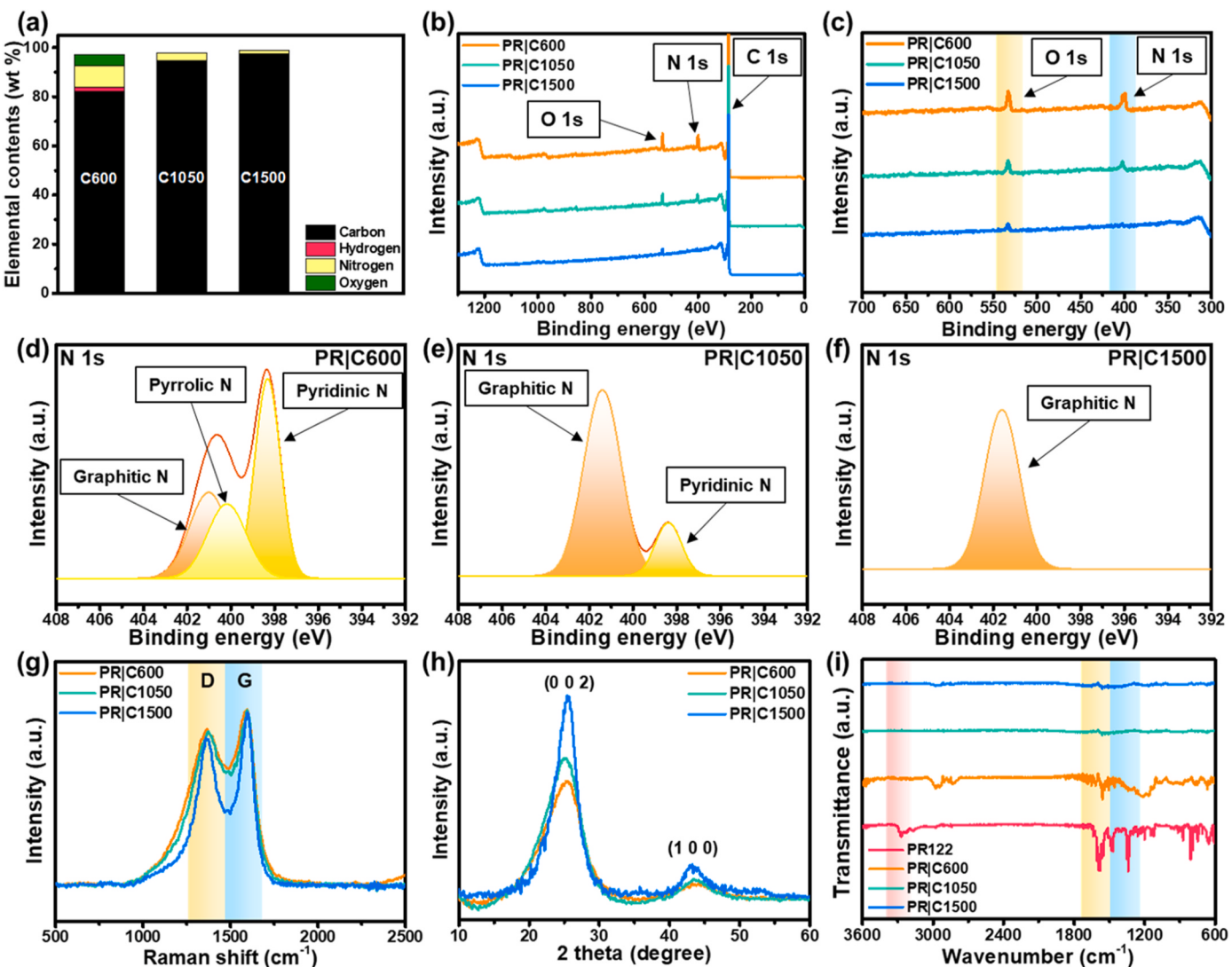


Fig. 3. Characterization. (a) Elemental composition of each sample. (b, c) XPS survey spectra of PR|C600, PR|C1050, and PR|C1500. (d–f) Deconvoluted XPS spectra of PR|C600, PR|C1050, and PR|C1500. (g) Raman spectra of PR|C600, PR|C1050, and PR|C1500. (h) X-ray diffraction patterns of PR|C600, PR|C1050, and PR|C1500. (i) FT-IR spectrum of PR122, PR|C600, PR|C1050, and PR|C1500.

pathways for ion transport. This structural transformation ultimately leads to improved electrochemical performance in LIBs. EIS measurements were conducted to compare the interfacial resistances of each electrode and plotted in Fig. 5c. The semi circles are attributed to the electrode-electrolyte interface charge transfer resistance (R_{CT}). The ohmic resistance of each cell has a similar value of 2.5Ω . In contrast, the R_{CT} value of PR|C1500 exhibits the lowest charge transfer resistance of 158Ω among the cells, due to its high crystallinity and excellent ionic conductivity. As shown in Fig. 5d–f, CV measurements were conducted at different scan rates ranging from 0.2 to 1.0 mV s^{-1} to evaluate the Li-ion diffusion kinetics of each cell. The relationship between peak current (i) and various scan rates (v) were analyzed using the following equation:

$$i = av^b \quad (9)$$

where a is a constant, and b can be obtained from the slope of the straight line of $\log(i)$ versus $\log(v)$. As the b value approaches 0.5 , it indicates that the diffusion-limited process is dominant during electrochemical reactions. Conversely, when b value is closer to 1 , the electrochemical behavior becomes more interface-limited and capacitive. The power law curves for each cell, obtained using equation (9), are

illustrated in Fig. 5g–i. The reduction slope values for PR|C600, PR|C1050, and PR|C1500 are 0.97 , 0.87 , and 0.83 , respectively. These values suggest that the diffusion-controlled process is highest in PR|C1500. Furthermore, the contributions of diffusion-controlled (k_1v) and capacitance-controlled ($k_2v^{1/2}$) processes can be quantitatively normalized using the following equation:

$$i = k_1v + k_2v^{1/2} \quad (10)$$

As shown in Fig. S3, the percentage contributions of the capacitive component to the capacity for PR|C600, PR|C1050, and PR|C1500 are 88.8% , 72.9% , and 51.7% at a scan rate of 0.2 mV s^{-1} , respectively. Moreover, PR|C1500 consistently demonstrates the highest diffusion contribution across various scan rates. These results suggest that the distinct crystal structure of PR|C1500 results in the highest Li-ion diffusion kinetics. As indicated by the findings, ionic conductivity and Li-ion diffusion in carbonized PR122 improve with increasing carbonization temperature. Fig. 5j–l shows the capacitive contribution of PR|C600, PR|C1050, and PR|C1500 at 1.0 mV s^{-1} . PR|C600 exhibits the highest value in capacitive contribution, illustrating the largest pseudocapacitive contribution region.

The electrochemical evaluation has substantially proven the potential of carbonized PR122 as an anode in LIBs. In addition, the obtained

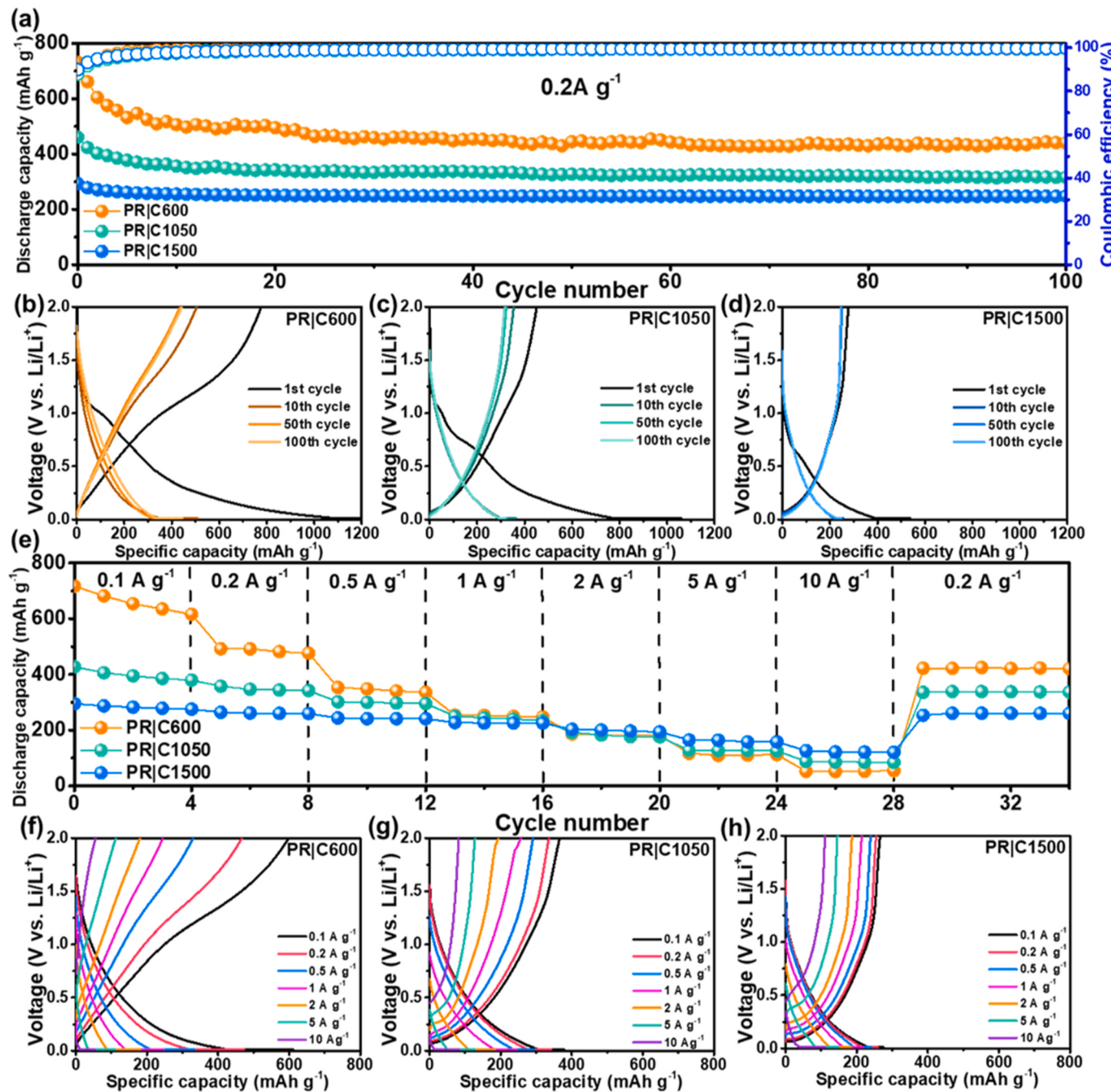


Fig. 4. Electrochemical performances in Li-ion battery system. (a) Cycle performance and (b–d) Voltage profiles of PR|C600, PR|C1050, and PR|C1500 at the 1st, 10th, 50th, and 100th cycles. (e) Rate capability and (f–h) voltage profiles of each electrode at different current densities.

results demonstrate how nitrogen content and carbon crystallinity, influenced by carbonization temperature, affect the electrochemical properties. In order to explore the potential of PR122-derived carbon as a separator-modifying material and to correlate carbon composition with the electrochemical stability of LMBs, each carbonized PR122 sample was coated onto the surface of PP separators and evaluated in Li/Cu asymmetric cells. The substantial effect of carbon-coated separators on improving the electrochemical stability of LMBs has been verified by the previous study [72]. Fig. 6a shows a cell configuration where the carbon layer (i.e., carbonized PR122) formed on the separator faces the current collector in the Li/Cu cell. The cycle performance of Li/Cu cells containing PP, PR|C600@PP, PR|C1050@PP, and PR|C1500@PP evaluated under conditions of 1 mA cm⁻² and 1 mAh cm⁻² is shown in

Fig. 6b. The reference cell, i.e., Li/Cu cell with PP, exhibits a gradual decline in Coulombic efficiency, dropping below 80 % at the 25th cycle and continuing to decline. The cell with PR|C1500@PP exhibits a sharp decrease in Coulombic efficiency after 75 cycles, and by the 100th cycle, its efficiency aligns closely with that of the reference cell (32.5 %). The cell with PR|C1050@PP exhibits a smaller decrease in Coulombic efficiency (48.1 %) over 100 cycles, while the cell with PR|C600@PP maintains a Coulombic efficiency of 70.0 % after 100 cycles. It can be inferred that the nitrogen-associated bonds, which serve as lithiophilic sites, within PR|C600 extend the cycle life of Li-metal batteries [73]. The voltage profiles of the first cycle and 100th cycle in Li/Cu cells with PP, PR|C600@PP, PR|C1050@PP, and PR|C1500@PP are presented in Fig. 6c–f, respectively. All the carbonized PR122 samples show the

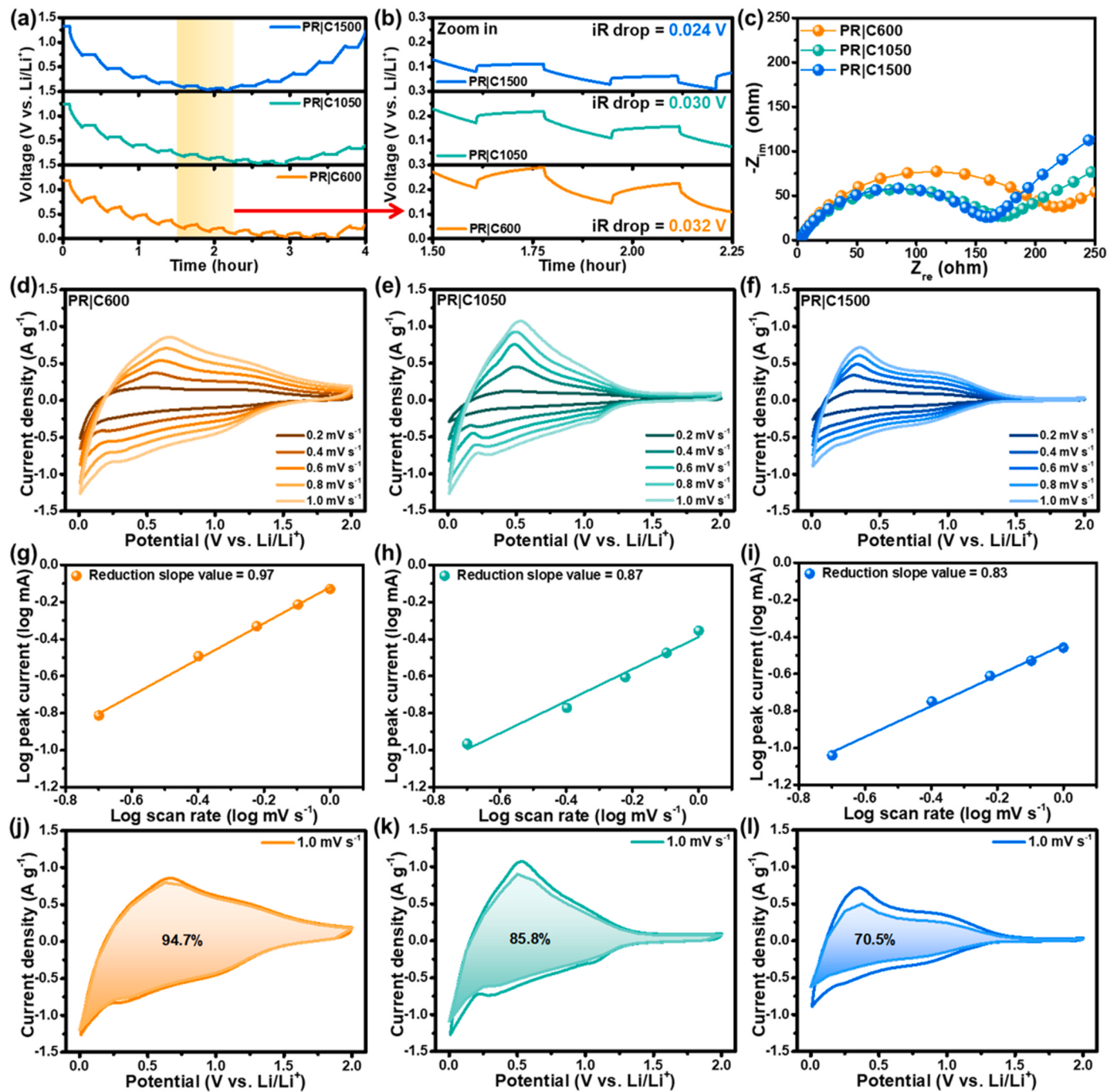


Fig. 5. Electrochemical kinetics of each carbon in the LIB system. (a, b) GITT curves of each carbonized PR122. (c) Nyquist plots after the initial cycle. (d–f) CV curves at scan rates of 0.2–1.0 mV s⁻¹. (g–i) Fitted lines between log(*i*) and log(*v*). (j–l) CV curves showing the marked capacitive contribution at 1.0 mV s⁻¹.

typical voltage region where Li is stored during lithiation. Especially, the cell with PR|C600@PP shows a relatively flatter sloping region during the delithiation process, likely due to the high nitrogen content of PR|C600. After cycling, the lithiation region observed in the first cycle disappears across all samples, but significant differences in Coulombic efficiency are observed for each electrode. The cell with PR|C600@PP retained 70.0 % of its initial Coulombic efficiency, while the cells with PR|C1050@PP and PR|C1500@PP exhibited a greater decrease in Coulombic efficiency after cycling. The changes in internal resistance of each cell before and after cycling are compared (Fig. 6g–j). The ohmic resistance of all the cells exhibits a similar value of approximately 4 Ω. The cells with PP separator, PR|C600@PP, PR|C1050@PP, and PR|C1500@PP exhibit the charge transfer resistance values of 320, 59, 47,

and 35 Ω, respectively, suggesting that PR|C600 relatively exhibits poor electron transfer ability due to the low degree of graphitization [74]. Interestingly, the cells with carbon-coated separators exhibit much lower charge transfer resistance in comparison to the cell with PP separator (Fig. 6g). This is attributed to the improved electrolyte wettability and electrolyte uptake [72,75]. Similar to the electrochemical results in the LIB system, the cell with PR|C1500@PP exhibits the lowest charge transfer resistance due to the highest ionic conductivity of PR|C1500. Although the cell with PR|C600 shows the highest charge transfer resistance among the cells, it achieved the most stable cycle performance while maintaining high coulombic efficiency. It can be inferred that the nitrogen content in the carbon scaffold plays a more dominant role in determining the cycle stability of LMBs than the

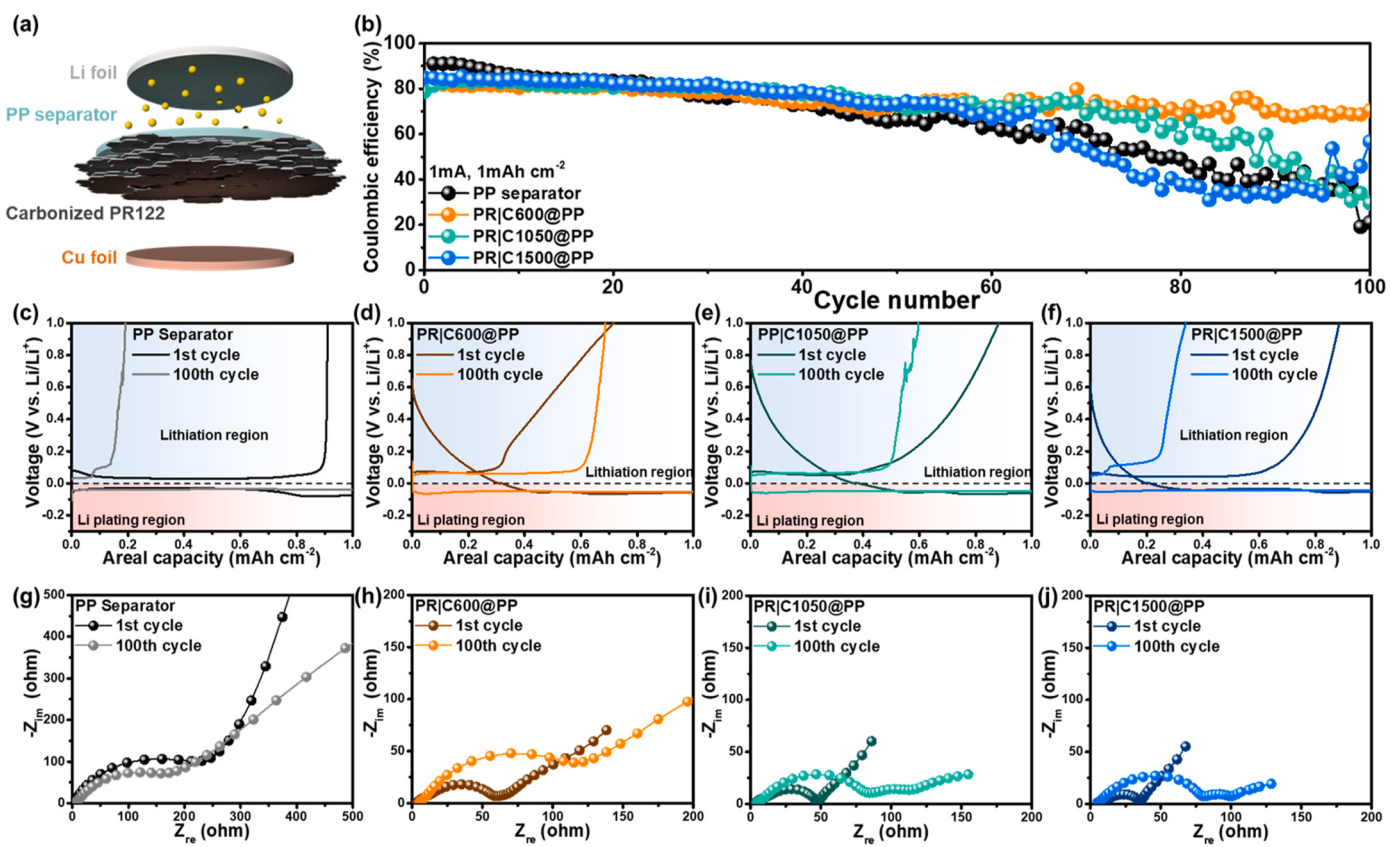


Fig. 6. Electrochemical performances in LMB system. (a) Schematic illustration of a cell configuration. (b) Cycle performances of Li/Cu cells with PP, PR|C600@PP, PR|C1050@PP, and PR|C1500@PP. (c–f) Voltage profiles and (g–j) Nyquist plots of each cell at 1st and 100th cycle.

conductivity of carbon.

In order to gain insight into the enhancement of lithiophilicity with different nitrogen content, the DFT calculations were utilized to compute the Li adsorption energies on the pristine graphene and N-rich graphene surfaces (Fig. 7a). The adsorption energies of Li on pristine graphene and graphitic N were calculated to be 1.15 eV and 1.04 eV, respectively. These positive values indicate weak interactions with Li, suggesting that Li adsorption is less favorable on these structures. In contrast, pyrrolic N and pyridinic N surfaces show potential as effective Li adsorption sites. The Li adsorption energy is calculated to be -2.58 eV for pyrrolic N and ranges from -0.96 to -3.18 eV for pyridinic N, depending on the N content. These results demonstrate that both pyrrolic N and pyridinic N exhibit lithiophilic properties that can significantly promote Li adsorption. This finding is consistent with the XPS results (Fig. 3d–f), which show that the decrease in lithiophilicity with increasing carbonization temperature. Thus, it is confirmed that the presence of N in the carbon structure, specifically pyrrolic N and pyridinic N, significantly improves lithiophilicity. Additionally, COMSOL Multiphysics was employed to investigate the effects of lithiophilicity on Li-deposition behaviors. In this simulation, thin layers with different diffusivities were placed at the interface between the electrolyte and the separator to represent the Li adsorption properties of the N-rich surface. The diffusivity was determined using adsorption kinetics of Langmuir isotherm model, according to the following equation [76]:

$$k_a \propto \exp\left(-\frac{E_{ads}}{RT}\right) \quad (11)$$

where k_a is the adsorption constant for the system, E_{ads} is the adsorption energy, and R is the gas constant. Using the diffusion coefficient of bare separator as the reference value of $5.58 \times 10^{-8} \text{ cm}^2 \text{ s}^{-1}$, the diffusion coefficients of each carbonized PR separator were determined through

the ratio of the adsorption energies calculated for pristine graphene and pyridinic N. The resulting diffusion coefficient is $4.09 \times 10^{-7} \text{ cm}^2 \text{ s}^{-1}$. The simulated morphologies of Li deposition with low and high lithiophilicity of separators are shown in Fig. 7b. The results show that the higher lithiophilicity of the separator contributes to even and slower flux of Li, promoting a homogeneous Li-deposition. This is consistent with the observed Li deposition behavior in the Li/Cu asymmetric cells, where the bare separator leads to relatively inhomogeneous Li deposition. Therefore, these findings clearly demonstrate that increasing the nitrogen content in the carbon structures significantly improves lithiophilicity, which promotes the uniform Li deposition. To further reveal the impact of carbon composition on the Li deposition behavior in LMBs, each cell with PR|C600@PP, PR|C1050@PP, and PR|C1500@PP was partially plated with Li. The surface morphology is examined to observe the deposition form of Li on the coating layer of each separator. In the case of PR|C600@PP, it shows homogeneous Li deposition over the carbon layer (Fig. 7c and f) [73]. In contrast, it exhibits relatively inhomogeneous Li deposition and the formation of Li dendrites in the case of PR|C1050@PP (Fig. 7d and g). Even more serious Li dendrite formation is observed on the PR|C1500@PP (Fig. 7e and h). Considering these results, it is confirmed that nitrogen-related bonds in the carbon significantly influences Li deposition behavior and electrochemical reversibility in LMBs, which is well consistent with the previous report [77]. Fig. S3 presents the N 1s XPS spectra of the PR|C600@PP, PR|C1050@PP, and PR|C1500@PP surfaces after cycling. These demonstrate that the negative shift of pyridinic, pyrrolic, and graphitic nitrogen occurs in comparison with the XPS results before cycling (Fig. 3d–f), due to the strong reaction between Li and nitrogen atoms [78].

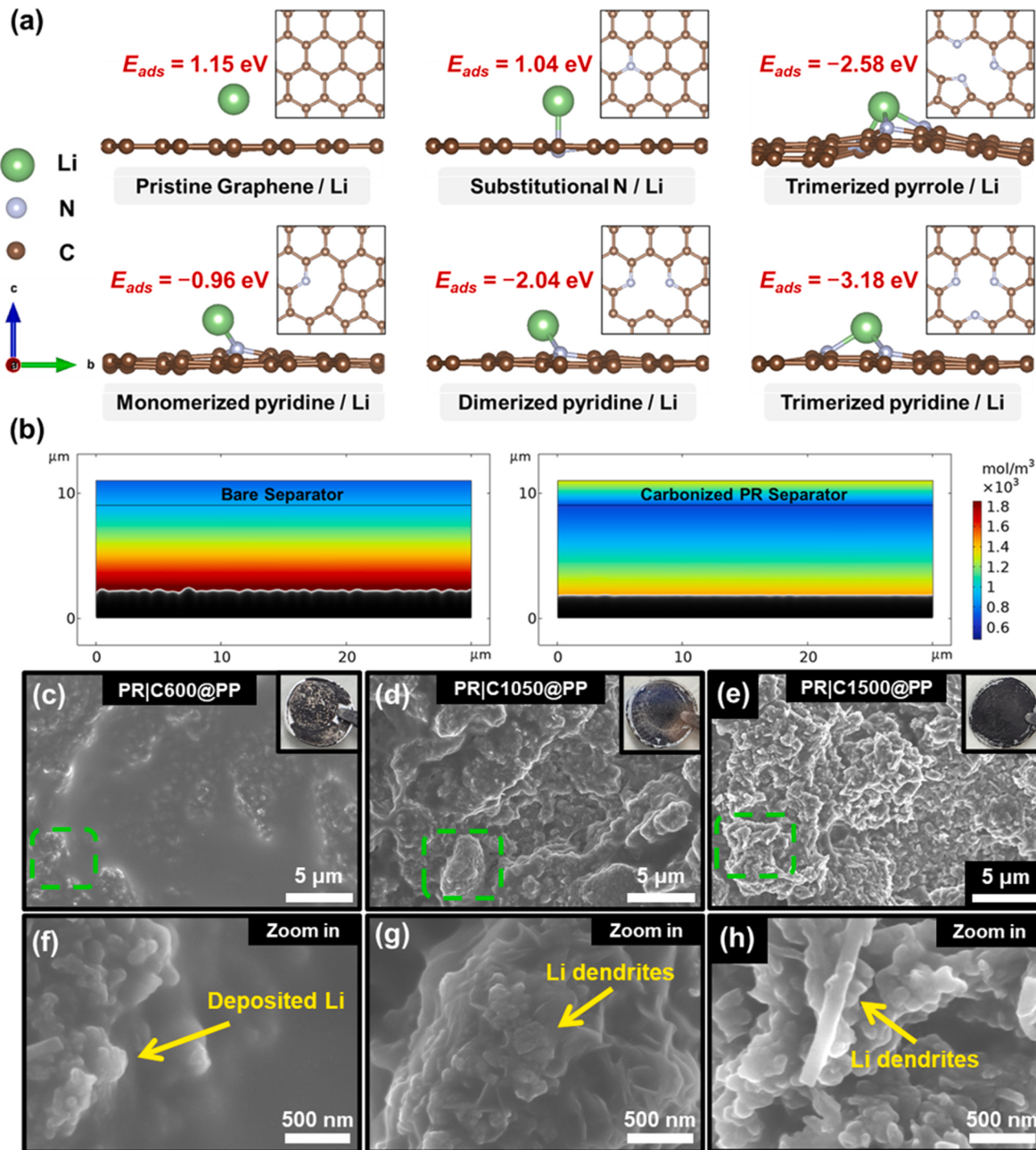


Fig. 7. DFT-based FEM analysis and post-mortem study. (a) Li adsorption energies on the surfaces of pristine graphene, graphitic N, Monomerized pyridine, Dimerized pyridine, Trimerized pyrrole. (b) Simulated morphology of Li deposition under bare separator and carbonized PR coated separator. SEM images of PR|C600@PP separator (c, f), PR|C1050@PP separator (d, g), and PR|C1500@PP separator (e, h) after cycles at low and high magnification.

4. Conclusions

In this article, the potential of PR122 as a carbonizable nitrogen-containing material was investigated in both Li-ion and Li-metal battery systems. In order to modulate the crystallinity and nitrogen content of the carbon, the carbonization temperature was controlled from 600 to 1500 °C. The carbonized PR122 was applied to the current collector for the LIB system and the separator for the LMB system. In LIBs, PR|C600 delivered the highest capacity of 440.2 mAh g⁻¹ at 0.2 A g⁻¹. In contrast, PR|C1500 exhibited excellent rate capability. These are attributed to the

relative nitrogen content in the carbon composition and the varying degrees of crystallinity of each carbonized PR122 sample. When it comes to the cycle stability in LMBs, the cell with PR|C600@PP delivered a much higher Coulombic efficiency of 70.0 % after 100 cycles, compared to the other cells (48.1 % for PR|C1050@PP and 32.5 % PR|C1500@PP). DFT-based FEM analyses and post-mortem SEM images have clearly demonstrated that nitrogen-associated bonds in the carbonized PR122 significantly affect the uniformity of Li deposition over the carbon layer and improve the long-term electrochemical reversibility in LMBs. The strategy of using organic pigments as

nitrogen-rich and carbonizable materials demonstrates potential for improving the rate performance in LIBs and extending the cycle life in LMBs. Furthermore, this study has elucidated that the electrochemical performance of LIBs and LMBs is highly influenced by both the nitrogen content and crystallinity of carbon-based materials. We strongly believe that designing nitrogen-containing carbonaceous materials from organic pigments can overcome a number of issues associated with traditional carbon and inspire more relevant research in next-generation batteries.

CRediT authorship contribution statement

Minsu Park: Writing – original draft, Visualization, Validation, Methodology, Formal analysis, Data curation, Conceptualization. **Kwonyun Lee:** Formal analysis, Data curation. **Min Sung Kang:** Writing – original draft, Visualization, Software, Data curation. **Sujeong Woo:** Methodology, Data curation. **Wootaek Choi:** Visualization, Data curation. **Hyein Kim:** Methodology. **Woong Kwon:** Methodology, Formal analysis, Data curation. **Junghyun Choi:** Resources, Data curation. **Sung Beom Cho:** Writing – original draft, Software, Formal analysis, Data curation. **Euigung Jeong:** Writing – review & editing, Supervision. **Patrick Joohyun Kim:** Writing – review & editing, Visualization, Supervision, Methodology, Conceptualization.

Declaration of competing interest

The authors declare that they have no known competing financial interests or personal relationships that could have appeared to influence the work reported in this paper.

Acknowledgement

This work was supported by the National Research Foundation of Korea (NRF) grant funded by the Korea government (MSIT) (RS-2023-00276626 and RS-2024-00428511).

Appendix A. Supplementary data

Supplementary data to this article can be found online at <https://doi.org/10.1016/j.carbon.2024.119870>.

References

- [1] J.A. Sanguesa, V. Torres-Sanz, P. Garrido, F.J. Martinez, J.M. Marquez-Barja, A review on electric vehicles: technologies and challenges, *Smart Cities* 4 (1) (2021) 372–404.
- [2] I. Husain, B. Ozpineci, M.S. Islam, E. Gurpinar, G.-J. Su, W. Yu, S. Chowdhury, L. Xue, D. Rahman, R. Sahu, Electric drive technology trends, challenges, and opportunities for future electric vehicles, *Proc. IEEE* 109 (6) (2021) 1039–1059.
- [3] H.S. Das, M.M. Rahman, S. Li, C.W. Tan, Electric vehicles standards, charging infrastructure, and impact on grid integration: a technological review, *Renew. Sustain. Energy Rev.* 120 (2020) 109618.
- [4] F. Wu, J. Maier, Y. Yu, Guidelines and trends for next-generation rechargeable lithium and lithium-ion batteries, *Chem. Soc. Rev.* 49 (5) (2020) 1569–1614.
- [5] M. Armand, P. Axmann, D. Bresser, M. Copley, K. Edström, C. Ekberg, D. Guyomard, B. Lestriez, P. Novák, M. Petraníkova, Lithium-ion batteries—Current state of the art and anticipated developments, *J. Power Sources* 479 (2020) 228708.
- [6] J.B. Goodenough, Rechargeable batteries: challenges old and new, *J. Solid State Electrochem.* 16 (2012) 2019–2029.
- [7] S. Zhao, Z. Guo, K. Yan, S. Wan, F. He, B. Sun, G. Wang, Towards high-energy-density lithium-ion batteries: strategies for developing high-capacity lithium-rich cathode materials, *Energy Storage Mater.* 34 (2021) 716–734.
- [8] C. Wang, C. Yang, Z. Zheng, Toward practical high-energy and high-power lithium battery anodes: present and future, *Adv. Sci.* 9 (9) (2022) 2105213.
- [9] X. Shen, H. Liu, X.-B. Cheng, C. Yan, J.-Q. Huang, Beyond lithium ion batteries: higher energy density battery systems based on lithium metal anodes, *Energy Storage Mater.* 12 (2018) 161–175.
- [10] D. Lin, Y. Liu, Y. Cui, Reviving the lithium metal anode for high-energy batteries, *Nat. Nanotechnol.* 12 (3) (2017) 194–206.
- [11] Z.A. Ghazi, Z. Sun, C. Sun, F. Qi, B. An, F. Li, H.M. Cheng, Key aspects of lithium metal anodes for lithium metal batteries, *Small* 15 (32) (2019) 1900687.
- [12] X.-B. Cheng, R. Zhang, C.-Z. Zhao, Q. Zhang, Toward safe lithium metal anode in rechargeable batteries: a review, *Chem. Rev.* 117 (15) (2017) 10403–10473.
- [13] J. Xiao, How lithium dendrites form in liquid batteries, *Science* 366 (6464) (2019) 426–427.
- [14] G. Liu, W. Lu, A model of concurrent lithium dendrite growth, SEI growth, SEI penetration and regrowth, *J. Electrochem. Soc.* 164 (9) (2017) A1826.
- [15] G. Bieker, M. Winter, P. Bieker, Electrochemical in situ investigations of SEI and dendrite formation on the lithium metal anode, *Phys. Chem. Chem. Phys.* 17 (14) (2015) 8670–8679.
- [16] B. Li, Y. Chao, M. Li, Y. Xiao, R. Li, K. Yang, X. Cui, G. Xu, L. Li, C. Yang, A review of solid electrolyte interphase (SEI) and dendrite formation in lithium batteries, *Electrochem. Energy Rev.* 6 (1) (2023) 7.
- [17] X. Zhang, A. Wang, X. Liu, J. Luo, Dendrites in lithium metal anodes: suppression, regulation, and elimination, *Accounts Chem. Res.* 52 (11) (2019) 3223–3232.
- [18] X. Gao, Y.-N. Zhou, D. Han, J. Zhou, D. Zhou, W. Tang, J.B. Goodenough, Thermodynamic understanding of Li-dendrite formation, *Joule* 4 (9) (2020) 1864–1879.
- [19] M.K. Aslam, Y. Niu, T. Hussain, H. Tabassum, W. Tang, M. Xu, R. Ahuja, How to avoid dendrite formation in metal batteries: innovative strategies for dendrite suppression, *Nano Energy* 86 (2021) 106142.
- [20] M.Z. Mayers, J.W. Kaminski, T.F. Miller III, Suppression of dendrite formation via pulse charging in rechargeable lithium metal batteries, *J. Phys. Chem. C* 116 (50) (2012) 26214–26221.
- [21] X. He, D. Bresser, S. Passerini, F. Baakes, U. Kreuer, J. Lopez, C.T. Mallia, Y. Shao-Horn, I. Čekić-Laskovic, S. Wiemers-Meyer, The passivity of lithium electrodes in liquid electrolytes for secondary batteries, *Nat. Rev. Mater.* 6 (11) (2021) 1036–1052.
- [22] J. Bae, H. Park, X. Guo, X. Zhang, J.H. Warner, G. Yu, High-performance magnesium metal batteries via switching the passivation film into a solid electrolyte interphase, *Energy Environ. Sci.* 14 (8) (2021) 4391–4399.
- [23] M.L. Meyerson, P.E. Papa, A. Heller, C.B. Mullins, Recent developments in dendrite-free lithium-metal deposition through tailoring of micro-and nanoscale artificial coatings, *ACS Nano* 15 (1) (2020) 29–46.
- [24] L. Ye, X. Li, A dynamic stability design strategy for lithium metal solid state batteries, *Nature* 593 (7858) (2021) 218–222.
- [25] K. Yoon, S. Lee, K. Oh, K. Kang, Challenges and strategies towards practically feasible solid-state lithium metal batteries, *Adv. Mater.* 34 (4) (2022) 2104666.
- [26] T. Zhang, W. He, W. Zhang, T. Wang, P. Li, Z. Sun, X. Yu, Designing composite solid-state electrolytes for high performance lithium ion or lithium metal batteries, *Chem. Sci.* 11 (33) (2020) 8686–8707.
- [27] A. Hu, W. Chen, X. Du, Y. Hu, T. Lei, H. Wang, L. Xue, Y. Li, H. Sun, Y. Yan, An artificial hybrid interphase for an ultrahigh-rate and practical lithium metal anode, *Energy Environ. Sci.* 14 (7) (2021) 4115–4124.
- [28] J. Lee, S.H. Jeong, J.S. Nam, M. Sagong, J. Ahn, H. Lim, I.D. Kim, Toward thin and stable anodes for practical lithium metal batteries: a review, strategies, and perspectives, *EcoMat* 5 (12) (2023) e12416.
- [29] J. Kim, G.R. Lee, R.B.K. Chung, P.J. Kim, J. Choi, Homogeneous Li deposition guided by ultra-thin lithiophilic layer for highly stable anode-free batteries, *Energy Storage Mater.* 61 (2023) 102899.
- [30] T.T. Zuo, X.W. Wu, C.P. Yang, Y.X. Yin, H. Ye, N.W. Li, Y.G. Guo, Graphitized carbon fibers as multifunctional 3D current collectors for high areal capacity Li anodes, *Adv. Mater.* 29 (29) (2017) 1700389.
- [31] S. Jo, K. Lee, Y. Jung, D. Woo, T. Kim, P.J. Kim, Direct-spun carbon nanotube sheet: a flexible, ultralight, stackable three-dimensional current collector for high-performance lithium-ion batteries, *Carbon* 219 (2024) 118786.
- [32] Y.K. Lee, K.Y. Cho, S. Lee, J. Choi, G. Lee, H.I. Joh, K. Eom, S. Lee, Construction of hierarchical surface on carbon fiber paper for lithium metal batteries with superior stability, *Adv. Energy Mater.* 13 (9) (2023) 2203770.
- [33] J. Kim, J. Choi, P.J. Kim, A new approach to stabilize the electrochemical performance of Li metal batteries through the structure alteration of CNT scaffolds, *Carbon* 203 (2023) 426–435.
- [34] S. Jin, Y. Jiang, H. Ji, Y. Yu, Advanced 3D current collectors for lithium-based batteries, *Adv. Mater.* 30 (48) (2018) 1802014.
- [35] S. Lee, S. Yang, K. Lee, Y. Jung, J. Choi, T. Kim, P.J. Kim, Dendrite-suppressed Li deposition enabled by surface-tailored carbon-based current collectors for high-rate and stable Li-metal batteries, *Carbon* (2024) 118941.
- [36] H.-J. Noh, M.-H. Lee, B.G. Kim, J.-H. Park, S.-M. Lee, J.-H. Choi, 3D carbon-based porous anode with a pore-size gradient for high-performance lithium metal batteries, *ACS Appl. Mater. Interfaces* 13 (46) (2021) 55227–55234.
- [37] T.-T. Zuo, X.-W. Wu, C.-P. Yang, Y.-X. Yin, H. Ye, N.-W. Li, Y.-G. Guo, Graphitized carbon fibers as multifunctional 3D current collectors for high areal capacity Li anodes, *Adv. Mater.* 29 (29) (2017) 1700389.
- [38] K. Kwon, J. Kim, K. Roh, P.J. Kim, J. Choi, Towards high performance Li metal batteries: surface functionalized graphene separator with improved electrochemical kinetics and stability, *Electrochim. Commun.* 157 (2023) 107598.
- [39] H.-H. Chang, T.-H. Ho, Y.-S. Su, Graphene-enhanced battery components in rechargeable lithium-ion and lithium metal batteries, *C* 7 (3) (2021) 65.
- [40] J. Duan, Y. Zheng, W. Luo, W. Wu, T. Wang, Y. Xie, S. Li, J. Li, Y. Huang, Is graphite lithiophobic or lithiophilic? *Natl. Sci. Rev.* 7 (7) (2020) 1208–1217.
- [41] H. Zhang, X. Liao, Y. Guan, Y. Xiang, M. Li, W. Zhang, X. Zhu, H. Ming, L. Lu, J. Qiu, Lithiophilic-lithiophobic gradient interfacial layer for a highly stable lithium metal anode, *Nat. Commun.* 9 (1) (2018) 3729.
- [42] X. Feng, H.-H. Wu, B. Gao, M. Świątostawski, X. He, Q. Zhang, Lithiophilic N-doped carbon bowls induced Li deposition in layered graphene film for advanced lithium metal batteries, *Nano Res.* 15 (1) (2022) 352–360.
- [43] X. Li, Z. Chu, H. Jiang, Y. Dai, W. Zheng, A. Liu, X. Jiang, G. He, Redistributing Li-ion flux and homogenizing Li-metal growth by N-doped hierarchically porous

- membranes for dendrite-free Lithium metal batteries, *Energy Storage Mater.* 37 (2021) 233–242.
- [44] M. Kim, S. Lee, D. Park, H. Kang, D. Kam, J.-H. Park, S.H. Oh, H.-G. Jung, W. Choi, Tuning lithiophilic sites of Ag-embedded N-doped carbon hollow spheres via intentional blocking strategy for ultrastable Li metal anode in rechargeable batteries, *ACS Sustain. Chem. Eng.* 11 (5) (2023) 1785–1796.
- [45] G. Huang, J. Han, F. Zhang, Z. Wang, H. Kashani, K. Watanabe, M. Chen, Lithiophilic 3D nanoporous nitrogen-doped graphene for dendrite-free and ultrahigh-rate lithium-metal anodes, *Adv. Mater.* 31 (2) (2019) 1805334.
- [46] X. Zhang, Y. Chen, F. Ma, X. Chen, B. Wang, Q. Wu, Z. Zhang, D. Liu, W. Zhang, J. He, Z.-L. Xu, Regulating Li uniform deposition by lithiophilic interlayer as Li-ion redistributor for highly stable lithium metal batteries, *Chem. Eng. J.* 436 (2022) 134945.
- [47] Y. Wang, J. Tan, Z. Li, L. Ma, Z. Liu, M. Ye, J. Shen, Recent progress on enhancing the Lithiophilicity of hosts for dendrite-free lithium metal batteries, *Energy Storage Mater.* 53 (2022) 156–182.
- [48] T. Jiang, K. Chen, J. Wang, Z. Hu, G. Wang, X.-D. Chen, P. Sun, Q. Zhang, C. Yan, L. Zhang, Nitrogen-doped graphdiyne nanowall stabilized dendrite-free lithium metal anodes, *J. Mater. Chem. A* 7 (48) (2019) 27535–27546.
- [49] T. Li, J. Jiang, H. Zhou, H. Shang, M. Huang, J. Gao, M. Qu, W. Liu, H. Zhang, G. Peng, Stabilizing Li metal anode by constructing lithiophilic N-doped carbon nanotubes on flexible carbon felt host, *Diam. Relat. Mater.* 130 (2022) 109391.
- [50] K.G. Hye, L.J. Yong, K.N. Rim, C. Yoon, J.-P. Kim, C.J. Hong, Preparation of red dyes derived from quinacridone pigment by introducing N-substituent and their characteristics as a colorant for LCD color filter, *Mol. Cryst. Liq. Cryst.* 563 (1) (2012) 36–42.
- [51] E. Kim, A.S. Lee, T. Lee, H.J. Seo, S. Chae, K. Kim, J.-W. Park, S.G. Lee, J.H. Lee, Organic dye-derived n, s Co-doped porous carbon hosts for effective lithium polysulfide confinement in lithium–sulfur batteries, *Nanomaterials* 11 (11) (2021) 2954.
- [52] T. Lee, W. Kwon, H. Kang, S. Chae, E. Kim, J. Kim, H.G. Chae, A.S. Lee, E. Jeong, J. H. Lee, S.G. Lee, Pyro-polymerization of organic pigments for superior lithium storage, *Carbon* 188 (2022) 187–196.
- [53] S. Chae, T. Lee, W. Kwon, H. Kang, H.J. Seo, E. Kim, E. Jeong, J.H. Lee, S.G. Lee, Longitudinally grown pyrolyzed quinacridones for sodium-ion battery anode, *Chem. Eng. J.* 453 (2023) 139805.
- [54] D. Liao, Y. Yang, J. Jia, Z. Liu, L. Fan, J.H. Xin, S. Han, X. Liu, A Nile red dye cathode with an asymmetric redox unit for lithium organic batteries, *Chem. Commun.* 60 (82) (2024) 11762–11765.
- [55] E. Reizer, B. Viskolcz, B. Fiser, Formation and growth mechanisms of polycyclic aromatic hydrocarbons: a mini-review, *Chemosphere* 291 (2022) 132793.
- [56] P. Chen, S. Fatayer, B. Schuler, J.N. Metz, L. Gross, N. Yao, Y. Zhang, The role of methyl groups in the early stage of thermal polymerization of polycyclic aromatic hydrocarbons revealed by molecular imaging, *Energy & Fuels* 35 (3) (2021) 2224–2233.
- [57] P.E. Blöchl, Projector augmented-wave method, *Phys. Rev. B* 50 (24) (1994) 17953–17979.
- [58] G. Kresse, J. Furthmüller, Efficient iterative schemes for ab initio total-energy calculations using a plane-wave basis set, *Phys. Rev. B* 54 (16) (1996) 11169–11186.
- [59] J.P. Perdew, K. Burke, M. Ernzerhof, Generalized gradient approximation made simple, *Phys. Rev. Lett.* 77 (18) (1996) 3865–3868.
- [60] S. Lakhera, M. Rana, K. Devlal, N. Kanagathara, J. Janczak, Photovoltaic characteristics of organic heterocyclic 2,9-dimethyl quinacridone in different solvents using DFT approach, *J. Photochem. Photobiol. Chem.* 441 (2023) 114664.
- [61] P. Yang, L. Ma, S. Bi, X. Xi, T. Huang, R. Liu, Y. Su, D. Wu, Superior anodic lithium storage behavior of organic pigment 2,9-dimethylquinacridone, *Chem. Eng. J.* 394 (2020) 124924.
- [62] M. Ilić, F.-H. Haegel, A. Lolić, Z. Nedić, T. Tostic, I.S. Ignjatović, A. Linden, N. D. Jablonowski, H. Hartmann, Surface functional groups and degree of carbonization of selected chars from different processes and feedstock, *PLoS One* 17 (11) (2022) e0277365.
- [63] Y. Tang, J. Chen, Z. Mao, C. Roth, D. Wang, Highly N-doped carbon with low graphitic-N content as anode material for enhanced initial Coulombic efficiency of lithium-ion batteries, *Carbon Energy* 5 (2) (2023) e257.
- [64] Y. Tang, X. Wang, J. Chen, X. Wang, D. Wang, Z. Mao, PVP-assisted synthesis of g-C3N4-derived N-doped graphene with tunable interplanar spacing as high-performance lithium/sodium ions battery anodes, *Carbon* 174 (2021) 98–109.
- [65] Z. Zhang, Y. Zhang, X. Mu, J. Du, H. Wang, B. Huang, J. Zhou, X. Pan, E. Xie, The carbonization temperature effect on the electrochemical performance of nitrogen-doped carbon monoliths, *Electrochim. Acta* 242 (2017) 100–106.
- [66] J. Li, X. Li, P. Zhao, D.Y. Lei, W. Li, J. Bai, Z. Ren, X. Xu, Searching for magnetism in pyrrolic N-doped graphene synthesized via hydrothermal reaction, *Carbon* 84 (2015) 460–468.
- [67] X. Liu, J. Zhang, S. Guo, N. Pinna, Graphene/N-doped carbon sandwiched nanosheets with ultrahigh nitrogen doping for boosting lithium-ion batteries, *J. Mater. Chem. A* 4 (4) (2016) 1423–1431.
- [68] S. Bu, N. Yao, M.A. Hunter, D.J. Searles, Q. Yuan, Design of two-dimensional carbon-nitride structures by tuning the nitrogen concentration, *npj Comput. Mater.* 6 (1) (2020) 128.
- [69] L. Liu, Y. Tian, A. Abdussalam, M.R.H.S. Gilani, W. Zhang, G. Xu, Hard carbons as anodes in sodium-ion batteries: sodium storage mechanism and optimization strategies, *Molecules* 27 (19) (2022) 6516.
- [70] M. Shandilya, S. Thakur, S. Thakur, Magnetic amendment in the fabrication of environment friendly and biodegradable iron oxide/ethyl cellulose nanocomposite membrane via electrospinning, *Cellulose* 27 (2020) 10007–10017.
- [71] L. Hilekelele, P.J. Franklyn, P.K. Tripathi, S.H. Durbach, Morphological and crystallinity differences in nitrogen-doped carbon nanotubes grown by chemical vapour deposition decomposition of melamine over coal fly ash, *RSC Adv.* 6 (80) (2016) 76773–76779.
- [72] M. Park, S. Woo, J. Seo, J. Choi, E. Jeong, P.J. Kim, Directing the uniform and dense Li deposition via graphene-enhanced separators for high-stability Li metal batteries, *Electrochim. Acta* 495 (2024) 144426.
- [73] X. Feng, H.-H. Wu, B. Gao, M. Świętłowski, X. He, Q. Zhang, Lithiophilic N-doped carbon bowls induced Li deposition in layered graphene film for advanced lithium metal batteries, *Nano Res.* 15 (2022) 352–360.
- [74] L. Li, P. Dai, X. Gu, Y. Wang, L. Yan, X. Zhao, High oxygen reduction activity on a metal–organic framework derived carbon combined with high degree of graphitization and pyridinic-N dopants, *J. Mater. Chem. A* 5 (2) (2017) 789–795.
- [75] J.R. Rodriguez, P.J. Kim, K. Kim, Z. Qi, H. Wang, V.G. Pol, Engineered heat dissipation and current distribution boron nitride-graphene layer coated on polypropylene separator for high performance lithium metal battery, *J. Colloid Interface Sci.* 583 (2021) 362–370.
- [76] M.A. Islam, M.A. Chowdhury, M.S.I. Mozumder, M.T. Uddin, Langmuir adsorption kinetics in liquid media: interface reaction model, *ACS Omega* 6 (22) (2021) 14481–14492.
- [77] X. Chen, X.-R. Chen, T.-Z. Hou, B.-Q. Li, X.-B. Cheng, R. Zhang, Q. Zhang, Lithiophilicity chemistry of heteroatom-doped carbon to guide uniform lithium nucleation in lithium metal anodes, *Sci. Adv.* 5 (2) (2019) eaau7728.
- [78] Z. Yang, Z. Yu, Y. Qu, X. Wang, W. Lu, T. Li, N. Chen, M. Yao, P. Gao, D. Zhang, Lithiophilic ZnSe nanoparticles/N-doped carbon for high energy density lithium metal batteries, *Chem. Eng. J.* 477 (2023) 147077.